

A SEARCH FOR UNRECOGNIZED CARBON-ENHANCED METAL-POOR STARS IN THE GALAXY

VINICIUS M. PLACCO

Departamento de Astronomia - Instituto de Astronomia, Geofísica e Ciências Atmosféricas, Universidade de São Paulo, São Paulo, SP 05508-900, Brazil

CATHERINE R. KENNEDY

Department of Physics & Astronomy and JINA: Joint Institute for Nuclear Astrophysics, Michigan State University, East Lansing, MI 48824, USA

SILVIA ROSSI

Departamento de Astronomia - Instituto de Astronomia, Geofísica e Ciências Atmosféricas, Universidade de São Paulo, São Paulo, SP 05508-900, Brazil

TIMOTHY C. BEERS, YOUNG SUN LEE

Department of Physics & Astronomy and JINA: Joint Institute for Nuclear Astrophysics, Michigan State University, East Lansing, MI 48824, USA

NORBERT CHRISTLIEB

Zentrum für Astronomie der Universität Heidelberg, Landessternwarte, Königstuhl 12, 69117, Heidelberg, Germany

THIRUPATHI SIVARANI

Indian Institute of Astrophysics, 2nd block, Koramangala, Bangalore 560034, India

DIETER REIMERS

Hamburger Sternwarte, Universität Hamburg, Gojenbergsweg 112, 21029 Hamburg, Germany

LUTZ WISOTZKI

Astrophysical Institute Potsdam, An der Sternwarte 16, 14482 Potsdam, Germany

(Accepted for publication in AJ – December 18, 2009)
Draft version January 14, 2010

ABSTRACT

We have developed a new procedure to search for carbon-enhanced metal-poor (CEMP) stars from the Hamburg/ESO (HES) prism-survey plates. This method employs an extended line index for the CH G-band, which we demonstrate to have superior behavior when compared to the narrower G-band index formerly employed to estimate G-band strengths for these spectra. Although CEMP stars have been found previously among candidate metal-poor stars selected from the HES, the selection on metallicity undersamples the population of intermediate-metallicity CEMP stars ($-2.5 \leq [\text{Fe}/\text{H}] \leq -1.0$); such stars are of importance for constraining the onset of the s-process in metal-deficient asymptotic giant-branch stars (thought to be associated with the origin of carbon for roughly 80% of CEMP stars). The new candidates also include substantial numbers of warmer carbon-enhanced stars, which were missed in previous HES searches for carbon stars due to selection criteria that emphasized stars with cooler temperatures.

A first subsample, biased towards brighter stars ($B < 15.5$), has been extracted from the scanned HES plates. After visual inspection (to eliminate spectra compromised by plate defects, overlapping spectra, etc., and to carry out rough spectral classifications), a list of 669 previously unidentified candidate CEMP stars was compiled. Follow-up spectroscopy for a pilot sample of 132 candidates was obtained with the Goodman spectrograph on the SOAR 4.1m telescope. Our results show that most of the observed stars lie in the targeted metallicity range, and possess prominent carbon absorption features at 4300 Å. The success rate for the identification of new CEMP stars is 43% (13 out of 30) for $[\text{Fe}/\text{H}] < -2.0$. For stars with $[\text{Fe}/\text{H}] < -2.5$, the ratio increases to 80% (4 out of 5 objects), including one star with $[\text{Fe}/\text{H}] < -3.0$.

Subject headings: Galaxy: halo – stars: abundances – stars: carbon – stars: Population II – techniques: spectroscopic – surveys

1. INTRODUCTION

The contemporary explosion of information arising from high-resolution spectroscopic studies of metal-poor stars in the Galaxy is re-shaping our understanding of the nature of the nucleosynthesis processes that took place during the early stellar generations. Among the most interesting are detailed follow-up observations of stars exhibiting large over-abundances of carbon ($+0.5 < [\text{C}/\text{Fe}] < +4.0$), an apparently common occurrence among metal-poor stars (Beers & Christlieb 2005).

It has been reported that a large fraction, at least 20%, of stars with metallicities $[\text{Fe}/\text{H}]^1 < -2.0$, exhibit large over-abundances of carbon ($[\text{C}/\text{Fe}] > +1.0$; Lucatello et al. 2006). The fraction of so-called carbon-enhanced metal-poor (CEMP) stars rises to 30% for $[\text{Fe}/\text{H}] < -3.0$, 40% for $[\text{Fe}/\text{H}] < -3.5$, and 100% for $[\text{Fe}/\text{H}] < -4.0$ (Christlieb et al. 2002; Frebel et al. 2005; Norris et al. 2007). However, there are also recent studies (e.g. Cohen et al. 2005; Frebel et al. 2006) claiming that this fraction is somewhat lower (9% and 14%, respectively). This variety of claims is one of the motivations for obtaining reliable determinations of metallicities and carbon abundances for a larger number of stars. Furthermore, the identification of (in particular, brighter) CEMP stars will play a major role in theoretical work on the subject (Herwig 2004; Campbell & Lattanzio 2008; Lau et al. 2009), as they will enable the high-resolution spectroscopic follow-up required to derive the abundance patterns of additional elements, and thereby test suggested astrophysical sites that might be associated with the carbon production.

The vast majority of known CEMP stars were originally identified as metal-poor candidates from objective-prism surveys, such as the HK survey of Beers and colleagues (Beers et al. 1985, 1992), and the Hamburg/ESO Survey (HES; Christlieb 2003; Christlieb et al. 2008), both of which were based on the presence of weak (or absent) lines of CaII. A list of HES stars with strong molecular lines of carbon has been previously published by Christlieb et al. (2001). Medium-resolution spectra for most of these objects have been obtained over the past few years (Goswami et al. 2006; Marsteller 2007). Inspection of these data indicate that at least 50% of these targets are consistent with identification as CEMP stars, while the others are roughly solar-metallicity carbon-rich stars. However, this previous set of carbon-rich candidates was selected based on the *sum* of molecular carbon lines, such as CN, C₂, and CH, which over-emphasizes cooler stars in the sample. CEMP stars with effective temperatures higher than about 5500 K often only exhibit unusual strengths of just a single carbon feature, the CH G-band at 4300 Å, and were likely to have been missed in the previous assembly. Since most previous CEMP stars have been discovered by targeting low-metallicity candidates, this has resulted in a biasing of the resulting samples of carbon-rich stars to $[\text{Fe}/\text{H}] < -2.5$; it would clearly be useful to extend the metallicity range for their discovery to higher values.

For most CEMP stars there exists a clear correlation between carbon enhancement and the presence

¹ $[\text{A}/\text{B}] = \log(N_A/N_B)_* - \log(N_A/N_B)_\odot$, where N is the number density of atoms of a given element, and the indices refers to the star (*) and the Sun (○).

of s-process-element over-abundances, such as for Ba (CEMP-s stars - see Beers & Christlieb 2005). Such behavior is consistent with the hypothesis that these enhancements (both for carbon and the s-process elements) are due to nucleosynthesis processes that took place during the asymptotic giant-branch (AGB - see Herwig 2005, for a detailed discussion) stage of evolution, either from the star itself (which should rarely be found, but see Masseron et al. 2006) or by a now-extinct binary companion that has transferred material to a surviving (observed) component (Stancliffe & Glebbeek 2008).

However, recent studies (e.g., Aoki et al. 2007) have shown that this correlation no longer persists (or at least is different in nature) for stars with $[\text{Fe}/\text{H}] < -2.7$, including all of the most iron-deficient stars known to date: HE 0107-5240 ([Fe/H]=-5.3; Christlieb et al. 2004), HE 1327-2326 ([Fe/H]=-5.4; Frebel et al. 2005) and HE 0557-4840 ([Fe/H]=-4.75; Norris et al. 2007). These so-called CEMP-no stars (indicating a lack of s-process-element over-abundances), and the other categories of CEMP stars that have been noted (Beers & Christlieb 2005), suggest that a variety of mechanisms for the production of carbon must have played a role in the early Universe. Furthermore, due to the aforementioned metallicity-dependent selection bias, many of the CEMP stars known to date may be associated with the outer-halo population, which exhibits a peak metallicity of $[\text{Fe}/\text{H}] \sim -2.2$ (Carollo et al. 2007). Additional CEMP stars that are likely to be associated with the inner-halo and metal-weak thick-disk populations, which extend to higher metallicities, are required to investigate possible differences in their origins (e.g., Frebel et al. 2006; Tumlinson 2007).

The primary goal of the present work is to demonstrate the efficacy of searching for intermediate-metallicity CEMP stars, through the use of a new approach for their identification. The inclusion of warmer carbon-enhanced candidates (which do not exhibit CN and C₂ bands) also enables investigations between the observed levels of carbon enhancement and evolutionary stage. It should also be kept in mind that the inventory of ultra ($[\text{Fe}/\text{H}] < -4.0$) and hyper ($[\text{Fe}/\text{H}] < -5.0$) metal-poor stars is likely to be incomplete. Even if some of those extreme objects might not present carbon enhancements, this work uses the available data as a support to find candidates that meet our expectations. Such extreme stars may have been overlooked in previous searches due to noisy spectra in the region of CaII K on objective-prism plates (see Christlieb et al. 2008, for an alternative procedure to overcome this issue), but they could reveal themselves by the presence of strong CH G-bands that are commonly associated with the most iron-deficient stars.

This paper is outlined as follows. The main features of the HES stellar database, and its specific application for the present work, are outlined in §2. Section 3 considers the flaws of the current line index used by the HES to quantify the strength of the CH G-band, and provides a definition of a new, extended line index for the G-band. The first HES subsample of candidate CEMP stars selected on the basis of this new index, and the criteria for candidate selection, are discussed in §4. Section 5 reports on medium-resolution follow-up spectra obtained with the SOAR 4.1m telescope for 132 CEMP candidates

in this pilot investigation, along with determinations of their atmospheric parameters (T_{eff} , $\log g$, [Fe/H]) and carbon abundances ([C/Fe]). Finally, our conclusions and perspectives for future observational follow-up are presented in §6.

2. THE HES DATABASE

The Hamburg/ESO Survey (Reimers 1990; Reimers & Wisotzki 1997; Wisotzki et al. 2000) was the first all-southern sky quasar survey. The main motivation for the survey was to find the brightest quasars in the southern hemisphere, both for statistical studies and to identify the best targets for follow-up absorption line spectroscopy. Due to the relatively high spectral resolution of the ESO Schmidt prism (15 Å at CaII K), it was expected that interesting species of stars, such as metal-poor halo stars, carbon stars, cataclysmic variables, white dwarfs, horizontal-branch stars, and others (see Christlieb et al. 2008, and references therein), could be found as a byproduct.

The HES prism survey was conducted with the 1m ESO Schmidt Telescope. With an effective area of 6726 deg², it covers all the extragalactic ($|b| > 30^\circ$) southern ($\delta < -2.5^\circ$) portion of the sky. Christlieb et al. (2008) used the survey to increase the number of metal-poor stars known, compared to the HK Survey, by a factor of about 3-5, mainly due to the fainter magnitudes achieved ($B \sim 17.5$). The total survey volume was increased by almost a factor of 10, relative to the HK survey, but follow-up observations have not yet been obtained for all of the most interesting HES candidates. The wavelength coverage of the HES spectra is 3200-5300 Å, which includes the CaII K line (3933 Å, suitable for [Fe/H] estimates - see Beers et al. 1999; Rossi et al. 2005) and the CH G-band (~ 4300 Å).

The present work (and additional investigations currently in progress) have made use of the full HES stellar database (4,404,908 objects). It is most helpful to work with a single and homogeneous sample of targets, in order to test our new index definitions and still have a relevant number of candidates for future analysis. Another important point is that the HES has had a number of published high-resolution studies that include CEMP stars (such as Barklem et al. 2005; Lucatello et al. 2006; Aoki et al. 2007; Schuler et al. 2008), which can be used for comparison.

3. GPE – A NEW LINE INDEX FOR CARBON

Previous medium-resolution spectroscopic analyses employed a 15 Å wide G-band index (GP), as defined by Beers et al. (1999); a similar index was originally defined by Beers et al. (1985), prior to the recognition that such large fractions of metal-poor stars would exhibit strong carbon enhancement.

The GP index is a pseudo-equivalent width that measures the contrast between the observed spectra and the continuum level. It is represented by the area enclosed in a 15 Å wide line-band, delimited by a psedo-continuum, which is calculated using a linear fit between the center values of two side-bands, on both blue and red sides of the line-band. Table 1 lists the wavelength ranges for some of the G-band indices found in the literature. The need for a new index is clear, as it has been shown in

TABLE 1
WAVELENGTH BANDS (Å) FOR CH G-BAND INDICES

Index	Blue sideband	Line band	Red sideband
GP ^a	4247.0-4267.0	4297.5-4312.5	4362.0-4372.0
GPHES ^b	4246.0-4255.0	4281.0-4307.0	4446.0-4612.0
GPE ^c	...	4200.0-4400.0	...

^a Beers et al. (1999).

^b Christlieb et al. (2008).

^c This work.

several studies (e.g. Rossi et al. 2005) that the 15 Å wide line band does not capture all of the flux absorbed by carbon-related features in the region of the CH G-band. In addition, the GP index suffers contamination of its sidebands when a given star is particularly carbon-rich, or at low effective temperatures, given that a linear fit severely underestimates the level of the continuum for those objects².

Christlieb et al. (2008) defined a new G-band index for use with the scanned HES spectra, GPHES, of width 26 Å, calibrated to be on a similar scale as the GP index. However, as can be appreciated from inspection of Figure 1, even this new, wider index is not sufficient for some of the more extreme CEMP candidates identified in the HES. A new index for this particular carbon feature should cover not only the classical G-band (centered at 4304 Å), but also the portion of the spectrum that extends out into the wings of the region, which is affected by other carbon features (such as C₂, which are often exhibited even by warmer CEMP stars). Note that even when a star does not have strong carbon (i.e., exhibits a weak or “normal” G-band), such an index should still remain valid, since there will not be much signal from other features inside the band (except for the H_γ Balmer line at 4340 Å; see below).

The GPE (GPHES Extended) index is defined as follows:

$$GPE = \int_{4200}^{4400} \left(1 - \frac{S(\lambda)}{C(\lambda)} \right) d\lambda \quad (1)$$

where $S(\lambda)$ represents the observed spectrum and $C(\lambda)$ is the local continuum. This definition is similar to that of Cardiel et al. (1998), but here we do not estimate the continuum level by side-band interpolations, since the presence of the carbon features can also affect those regions and thereby compromise the index. We experimented with a variety of fitting approaches for the continuum, including the same procedures originally adopted for the GP and GPHES indices. The final choice is based on the techniques employed by the SEGUE Stellar Parameter Pipeline (SSPP - see Lee et al. 2008a,b; Allende Prieto et al. 2008, for a detailed description of the procedure), adjusted to work at the resolution of the HES spectra.

Figure 1 shows a typical (cool) carbon-enhanced star spectrum from the scanned HES plates. The narrow area around 4300 Å shows the location of the GPHES index,

² See Figures 1(h) and 2(d) of Rossi et al. (2005).

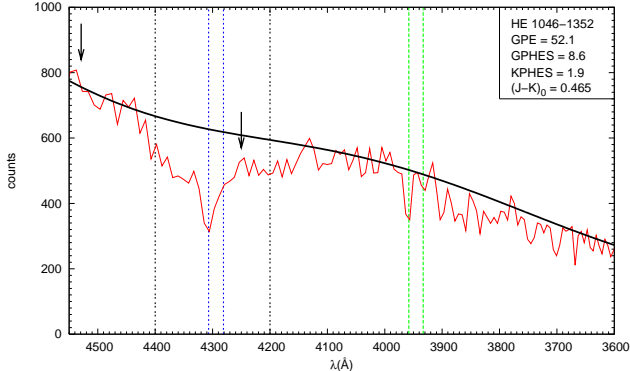


FIG. 1.— Example of the new G-band index definition. The solid (black) line shows the continuum fitting applied to the stars in this work. The long-dashed (green) lines represent the CaII H and K features. Also shown is the comparison between the GPHES (blue dotted lines) and the newly defined GPE (black dashed lines) line bands. The arrows represent the center values of the GPHES continuum sidebands. Note that the wavelength axis is plotted red to blue, as in the original HES scans.

which is wider (and shifted slightly to the blue region) than the GP index. The new GPE index line band is represented by the 200 Å wide region around the same location. Figure 1 shows that the GPHES index band is too narrow to be representative of the strength of the entire feature, and its sidebands are contaminated as well. Similar comments apply to the GP index.

From our own inspection, the optimal definition of the new index covers the range 4200–4400 Å. The GPE index does encompass the H_γ Balmer line at 4340 Å, but this should not represent a problem, since this Balmer line will be present in carbon-normal stars as well; its strength should scale in the same way with temperature for both carbon-normal and carbon-rich stars. In the definition of GPE, the continuum shape plays an especially important role, since it must be well-fit over the entire region (rather than estimated from more isolated sidebands).

4. SELECTION OF CEMP CANDIDATES

The main goal of this pilot study is to test the new GPE index with the HES database, by comparing its ability to select CEMP stars with available high-resolution analysis (and hence known atmospheric parameters, and [C/Fe]; e.g. Aoki et al. 2007) that are similar to the new stars we seek to identify for future follow-up survey efforts. We begin by obtaining GPE indices for a selected subsample of HES candidates, as well as for the HES stars studied by Aoki et al. (2007), and examine their behavior in a GPE versus (J–K)₀ diagram, where the near-infrared photometry is taken from 2MASS (Skrutskie et al. 2006). Because most of the stars will be “carbon-normal” (meaning the strength of the CH G-band scales with metallicity), rather than CEMP stars, one can then identify the locus of stars with enhanced carbon based on their deviation from the trend associated with carbon-normal stars.

4.1. First HES Subsample

To identify our initial candidates, the following criteria were applied to the HES database:

- ph_qual = AAA (accurate JHK photometry from 2MASS);

- objtype = stars (removes extended and bright sources);
- KPHES < 8.0 (removes stars with clearly too strong CaII K lines for a metal-poor star, regardless of their effective temperature);
- BHES < 15.5 (bright-object selection, for observations with the SOAR telescope);
- $0.15 \leq (J-K)_0 \leq 0.90$ (color range suitable for abundance analysis).

This first set of constraints yielded 85894 raw candidates. The GPE index was calculated for those candidates, as well as for low-resolution spectra of the HES stars in Aoki et al. (2007), which are confirmed CEMP stars. Figure 2 shows the distribution of the GPE index, as a function of (J–K)₀ color, for the raw candidates (small gray dots) and for the Aoki et al. (2007) stars (black filled circles). The (J–K)₀ color was chosen as a proxy for temperature, since this variable greatly influences the strength of molecular carbon features, such as CN, C₂, CH, as well as the hydrogen Balmer lines. The index works because, for a given value of (J–K)₀, the CEMP stars will have higher GPE values than the ones without enhancements.

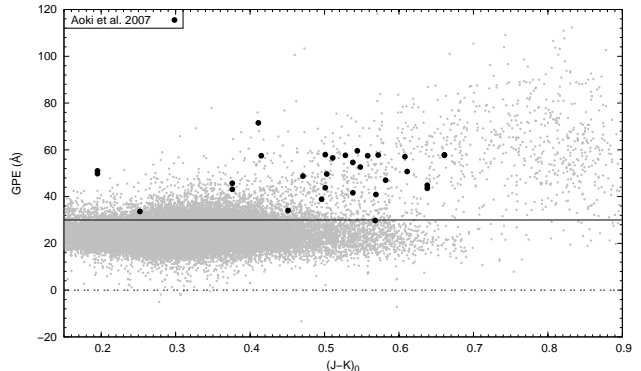


FIG. 2.— Distribution of the new line index, as a function of the (J–K)₀ color, for the 85,894 candidates (small gray dots) and stars from Aoki et al. (2007) (black filled circles). The solid line shows the lower limit of GPE.

Based on the location of the known carbon-enhanced stars on this diagram, relative to the locus of carbon-normal stars, a lower limit on GPE was set at 30 Å, reducing the number of candidates to 6018 stars. We are aware that possible candidates may be missed by this restriction, but this value is a compromise between obtaining a satisfactory number of candidates to explore for new CEMP stars and the time spent on the follow-up observations. If the limiting value was chosen at GPE = 35, the yield would be only 1883 candidates. Similarly, going as low as GPE = 25, the number would rise to 26313 candidates.

One of the primary reasons for the use of a new index is that the GPHES index, as it is calculated for the HES stars, is likely to be saturated, or have its sidebands contaminated from strong carbon features. Figure 3 shows the values for both indices for the first subsample. One

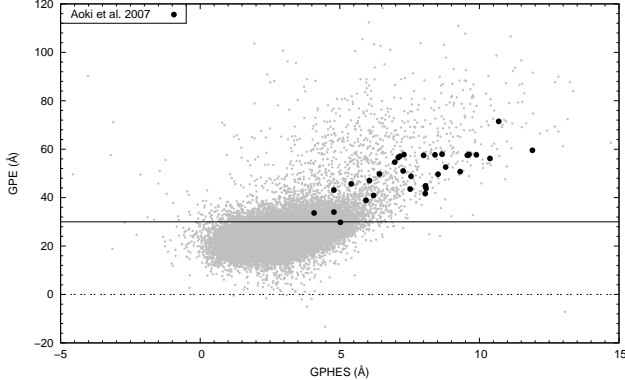


FIG. 3.— Comparison between the GPHEs index previously calculated for the HES stars and the new GPE index. The filled black circles are stars from Aoki et al. (2007).

can clearly notice that a deviation from a linear relation between the two indices occurs, especially for the higher values of GPE (which are also the stars with redder $(J-K)_0$, as seen in Figure 2). It is also obvious that the GPE index enjoys a greater dynamical range than the GPHEs index, which is crucial when one considers the effects of errors on the measurement of these indices. Small measurement errors impact the GPHEs index far more than the GPE index is expected to be perturbed (owing to its larger width and better-defined continuum).

Since the restrictions made above do not take into account any cuts on S/N ratio, nor can they distinguish between satisfactory measurements of HES spectra and possible difficulties due to plate artifacts, overlapping spectra, etc., a careful inspection of each prism spectrum is necessary, as discussed below.

4.2. Visual Inspection

To validate the index calculations, a visual inspection of the digitized HES spectra was made for candidate stars with $GPE \geq 30 \text{ \AA}$ in order to: (1) assign classifications to the stars based on the strength of the CaII K line and the presence of hydrogen Balmer lines, or clear molecular carbon bands and (2) rule out spurious values of GPE originating from overlapping spectra, emulsion scratches, or border effects on the photographic plates. Table 2 lists the distribution of the sample of 6018 candidates, according to the main assigned classes. The behavior of the new index for all classes (excluding low S/N spectra and errors due to overlaps and artifacts on the photographic plates) is shown in Figure 4.

From inspection of Figure 4, the majority of stars on the blue end of the $(J-K)_0$ scale exhibit strong hydrogen lines. They came into the sample due to the fact that the strong H_{γ} line (4340 \AA) contributes significantly to the GPE line index. For redder colors, $(J-K)_0 > 0.3$, the strength of the Balmer line decreases with temperature, so the enhancement of the line index is no longer a serious issue. On the red end of the color scale, one sees that the *unid* stars are concentrated in the $(J-K)_0 > 0.7$ region. These are cool stars, with little signal in the blue end of the spectrum, hence it is difficult to identify (and estimate the strength of) the CaII K line on the original prism spectra.

TABLE 2
VISUAL INSPECTION CLASSIFICATION FOR THE SELECTED CANDIDATES

Tag	Description	Candidates
mpca	Absent CaII K line	4
mpcb	Weak CaII K line	280
mpcc	Strong CaII K line	4614
unid	CaII K line not found	143
fhlc	Faint high latitude carbon stars	30
habs	Strong absorption H lines	73
hbab	Horizontal-branch/A type star	218
nois	Low signal-to-noise ratio	277
ovl	Overlapping spectra	79
art	Artifacts on photographic plates	123

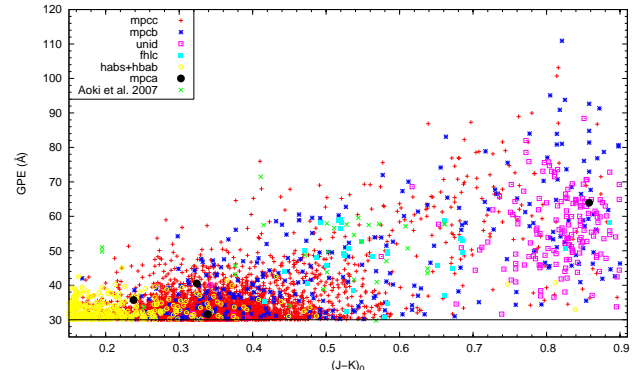


FIG. 4.— Index-color diagram for the 6018 candidates that were subject to visual inspection, divided according to the classes defined in Table 2. The Aoki et al. (2007) stars are indicated by green crosses.

4.3. The Index-Color Selection

One difficulty with the selection described above is that the candidate sample is dominated by a large number of stars with strong CaII K features, many of which may be more metal-rich than the CEMP stars we seek to identify. To reduce the number of these objects, we adopt a relaxed version of the selection of Christlieb et al. (2008) in the KP³ index versus $(J-K)_0$ or BVHES color parameter space. A metallicity cutoff of $[\text{Fe}/\text{H}] = -2.0$, instead of the $[\text{Fe}/\text{H}] = -2.5$ limit used by the HES metal-poor star selection, was chosen. Note that errors in the measurement of the KP index ensures that (due to their great numbers) many stars with $-2.0 \leq [\text{Fe}/\text{H}] \leq -1.0$ will still enter our sample. Had we raised the cutoff in the selection closer to $[\text{Fe}/\text{H}] \sim -1.0$, the numbers of higher-abundance stars would become prohibitive. Figure 5 shows the distribution of stars with strong CaII K lines (*mpcc*) for both colors and the adjusted polynomials.

The final selection of CEMP candidates includes all stars with absent (*mpca*), weak (*mpcb*) or not found (*unid*) CaII K lines, objects with strong carbon molecular bands (*fhlc*), and also the *mpcc* stars with KP indices that are below at least one of the KP cutoffs (gray dots on Figure 5). After this step, a search was performed on the full candidate list, and all of the already-known objects (from previous HES selection, including the metal-poor

³ The KP line index measures the strength of the CaII K line, defined by Beers et al. (1999).

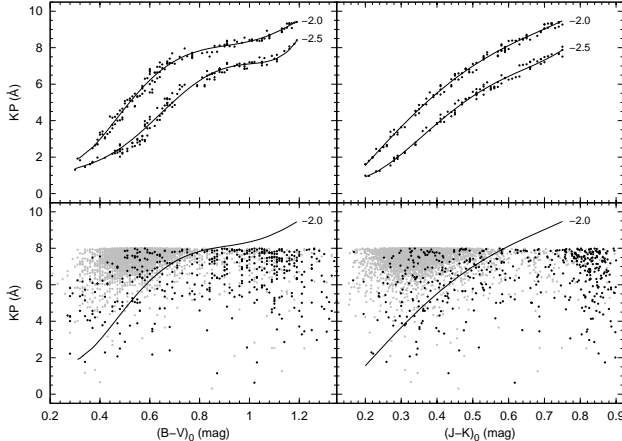


FIG. 5.— Upper panels: Polynomial adjustments for constant values of $[Fe/H]$, based on Christlieb et al. (2008). Lower panels: Selection criteria to eliminate strong CaII K line stars ($mpcc$). The black dots represent the stars with absent ($mpca$), weak ($mpcb$) or not found ($unid$) CaII K lines. The gray dots represent the $mpcc$ stars and the ones below the $[Fe/H] \leq -2.0$ line for at least one of the color indices are selected.

stars and known carbon-enhanced stars) were removed. This procedure yielded a list of 669 CEMP newly identified candidate CEMP stars.

5. VALIDATION OF THE CEMP CANDIDATES

Validation of our selected CEMP candidates is an important part of this pilot study. For this purpose we have obtained medium-resolution optical spectra for a limited number of CEMP candidates with the SOAR 4.1m telescope. After gathering and reducing the data, we obtained first-pass estimates of the stellar atmospheric parameters using the SSPP and a separate procedure to measure $[C/Fe]$. Details of the observations, reduction procedures, and further analysis are provided below.

5.1. Medium-Resolution Spectroscopic Observations

Medium-resolution spectra for the first 132 of our 669 CEMP candidates were obtained with the new Goodman high-throughput spectrograph on the SOAR 4.1m telescope, over the course of early science verification for this instrument. The Goodman spectrograph operates with several different observing modes. We employed the 600 l/mm grating in the blue setting (wavelength range 3550–5500 Å) with a 1.03" slit. This resulted in a resolving power of $R \sim 1500$ (resolution of ~ 3.5 Å). This resolution was chosen due to its similarity to spectra obtained during the Sloan Digital Sky Survey (York et al. 2000), for which the SSPP was designed to work.

The calibration frames include biases, quartz flats, as well as HgAr and Cu arc lamp exposures taken following each program object's observation. The exposure times for most of the observed stars were in the range of 10–20 minutes (targeting an “as-observed” $S/N > 40$ in the region of the CH G-band). Bias subtraction, flat-field correction, spectral extraction, wavelength calibration, and continuum normalization were all performed using standard IRAF packages. Table 3 lists the equatorial coordinates, BHES magnitude, $(J-K)_0$, GPE, KPHES, GPHES, and the classifications for our sample. The spectra for some of the observed stars are shown in Figures 6–8, organized by increasing $(J-K)_0$ color values.

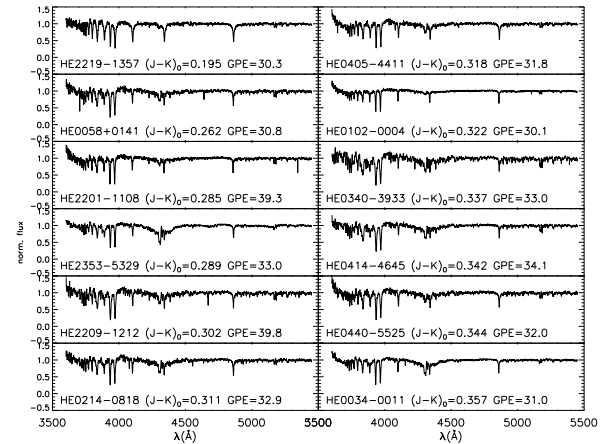


FIG. 6.— Example of CEMP candidates observed based on the new line index criteria. The spectra were taken with Goodman spectrograph on the SOAR telescope.

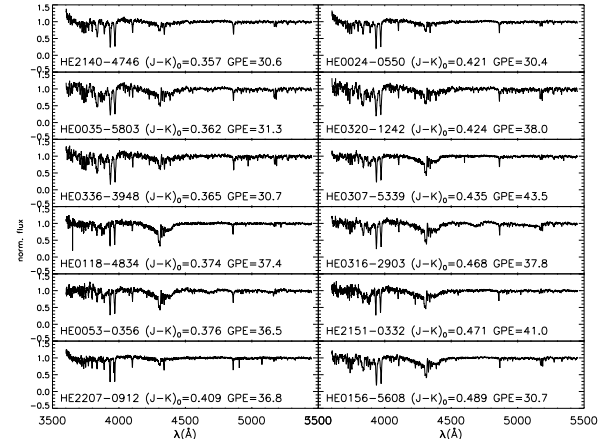


FIG. 7.— Example of CEMP candidates observed based on the new line index criteria. The spectra were taken with Goodman spectrograph on the SOAR telescope.

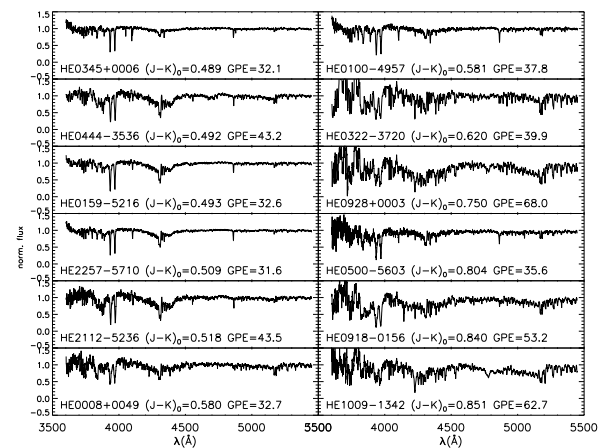


FIG. 8.— Example of CEMP candidates observed based on the new line index criteria. The spectra were taken with Goodman spectrograph on the SOAR telescope.

5.2. Atmospheric Parameter Estimates and Carbon Abundances

We employed the SSPP to obtain first-pass atmospheric parameter estimates for the observed CEMP candidates; the results are listed in Table 4. The last two columns refer to the carbon abundance ratios and estimated errors, respectively, obtained by the procedures discussed below.

The radial velocities calculated for the standard stars in our program presented unexpectedly large errors (on the order of 50 km/s), which we suspect are due to poorly corrected flexure of the Goodman spectrograph during commissioning. We used different techniques for this procedure (including line-by-line estimates and cross-correlation analysis) to assure that large-than-desired errors were not due to analysis issues. Since the velocities for the program stars are not known in advance, similar errors are expected. This does not present a major issue for our particular application, since the SSPP requires only a rough estimate of the radial velocity to perform its calculations. However, it would clearly be desirable to improve the derived velocity errors for future work.

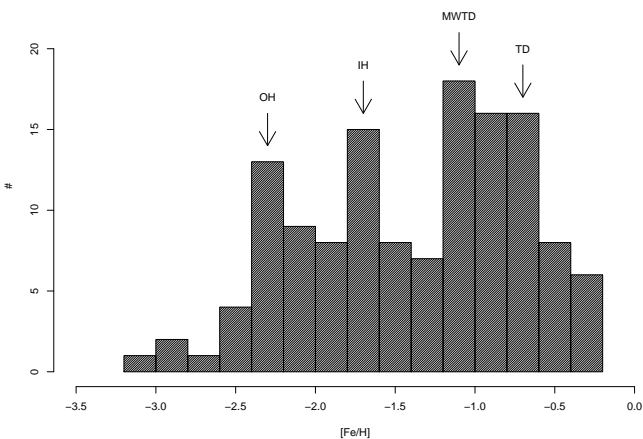


FIG. 9.— Metallicity distribution for the observed candidates. The arrows indicate the location of the peak metallicities in the observed distribution, which are rather close to those associated by Carollo et al. (2007) with the outer-halo (OH; $[Fe/H] = -2.2$), inner-halo (IH; $[Fe/H] = -1.6$), metal-weak thick disk (MWTD; $[Fe/H] = -1.3$) and canonical thick-disk (TD; $[Fe/H] = -0.6$) populations. Bins are 0.2 dex in width.

Figure 9 shows the observed metallicity distribution for the stars in Table 4. It is interesting to note that the two prominent peaks at low metallicity lie rather close to the peak metallicities that Carollo et al. (2007) associate with the outer-halo ($[Fe/H] = -2.2$) and inner-halo ($[Fe/H] = -1.6$) populations. Additional stars that may be associated with the metal-weak and canonical thick-disk populations are evident at higher metallicity. We conclude that we are, in fact, obtaining new CEMP stars distributed over our targeted metallicity range.

Trends of the GPE index with derived metallicity are presented in Figure 10. This figure also shows the relationship between the high-resolution $[Fe/H]$ obtained

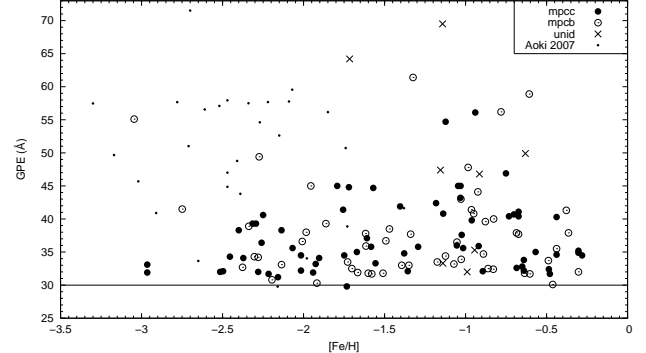


FIG. 10.— Behavior of the metallicity with the GPE index for the observed candidates and for the stars from Aoki et al. (2007).

by Aoki et al. (2007) and the GPE index, calculated directly from the HES prism spectra. There is no apparent distinction between the regimes for *mpcb* and *mpcc* stars. Also, as expected, the metallicities greater than -0.5 seen in Figure 10 belong to the stars with higher temperatures. In fact, one of the main purposes of this work is to find CEMP with metallicities greater than $[Fe/H] = -2.5$, in order to fill out the upper-right portion of Figure 10.

For the estimation of carbon abundances, we generated an extensive grid of synthetic spectra covering wavelengths between 3600–4600 Å. The stellar parameters of the grid covers T_{eff} from 3500 to 9750 K, $\log g$ from 0.0 to 5.0 and $[Fe/H]$ from -2.5 to 0.0 . The carbon abundances ($[C/H]$) ranges between $[Fe/H] - 0.5 \leq [C/H] \leq +0.5$, for a given value of $[Fe/H]$. We employed Kurucz NEWODF models (Castelli & Kurucz 2003) and the current version of the spectrum synthesis code *turbospectrum* (Alvarez & Plez 1998) for generating the synthetic spectra. The linelists used are the same as in Sivarani et al. (2006).

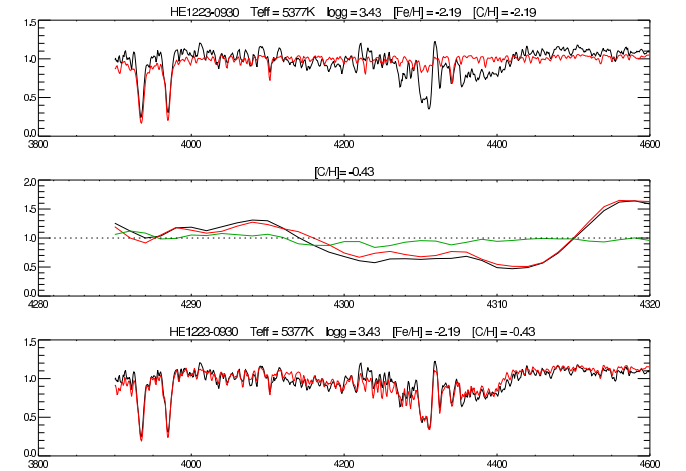


FIG. 11.— Example of carbon abundance determination for one of the stars in our sample. The upper panel shows a portion of the original spectrum (black) overlaid with a synthetic spectrum (red) with the listed parameters and $[C/Fe] = 0.0$. The middle panel shows the region around the CH G-band, with a red line showing the best fit. The green line is a division of the original spectrum by the fit spectrum, which should be close to 1.0 for a successful fit. The lower panel shows the result of the best fit with the listed $[C/H]$.

Estimation of carbon abundance was accomplished us-

ing chi-square minimization of the observed and synthetic spectra, in the wavelength region between 4285–4320 Å. The initial guess value for [C/H] was the same as [Fe/H] (given by the SSPP), i.e., a solar [C/Fe]. An example fit to the CH G-band region, which is the feature used to estimate [C/Fe], is shown in Figure 11. Only the carbon abundance is changed; all the other stellar parameters are kept constant and chi-square was estimated, using the IDL AMOEBA routine (down-hill Simplex) for optimization. In most cases the procedure converged to an adequate fit, by which we mean the chi-square of the residuals was more than a one-sigma improvement over the initial (solar) estimate; the typical error bar associated with this situation is on the order of $\delta_{[C/Fe]} = 0.1$ dex. In other cases, although the routine converged, the level of improvement did not reach the one-sigma level. In these instances we assign errors of 0.2 dex. These determinations of [C/Fe], and their errors, are listed in the last two columns of Table 4. To test that the reported value for [C/Fe] is a detection, rather than an upper limit, we further demand that the integrated line strength in a 20 Å band (from 4295 Å to 4315 Å) be at least 1.5 Å. This value was settled upon by comparison with noise-injected synthetic spectra with a variety of input fixed [C/Fe]. Determinations of [C/Fe] that failed to meet this criterion are considered upper limits, and are reported in Table 4 without listed errors.

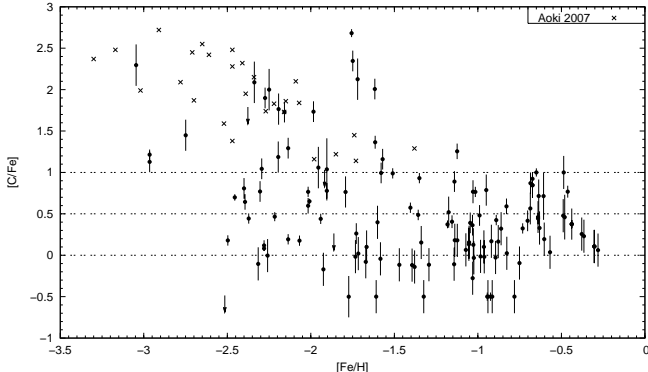


FIG. 12.— Behavior of the metallicity with the carbon abundance [C/Fe] for the observed candidates and for the stars from Aoki et al. (2007). The arrows represent upper limits. The dashed lines show constant values of [C/Fe] (0.0, +0.5 and +1.0).

Figure 12 shows the behavior of the carbon abundances as a function of metallicity, including the high-resolution measurements from Aoki et al. (2007). As already pointed out by other studies (Rossi et al. 2005; Lucatello et al. 2006), there is a clear trend in the [C/Fe] ratios, which are higher for lower metallicities, and exhibit increasing scatter for $[Fe/H] < -2.0$. This behavior is seen as well for the high-resolution data shown in the figure.

By using our new selection method, which it should be recalled is biased towards finding stars with higher carbon abundance, the fraction of carbon-enhanced stars (considering the error bars in [C/Fe]), is $\sim 25\%$. If one considers only the very metal-poor stars ($[Fe/H] < -2.0$), the fraction increases to 43%. For the five observed candidates that present estimated metallicities significantly lower than $[Fe/H] = -2.5$, our method reached

80% success. It is worth noting that the majority of metal-poor stars in our candidate pool with $[Fe/H] < -1.0$ (51%) present considerable carbon enhancements ($[C/Fe] > +0.5$).

6. CONCLUSIONS

We have developed a new line index for the region of the carbon G-band at 4304 Å, GPE, which has the advantage of capturing more information concerning the abundance of carbon, since its width takes into account the wings of the band, which includes other nearby carbon features. Furthermore, it is not subject to confounding (as were previously employed narrower indices) due to sidebands that fall in regions of the spectrum for which carbon features are present. To test this new method, we obtained a sample of stars from the HES stellar database, and compared the newly calculated index with the ones for confirmed carbon-rich stars based on high-resolution analysis (Aoki et al. 2007). Medium-resolution spectra for a sample of 132 stars selected by this procedure have been obtained with the Goodman spectrograph on the SOAR 4.1m telescope. Our new selection technique achieves a success rate for newly identified CEMP stars of 43% for stars with $[Fe/H] < -2.0$; four out of five candidates with $[Fe/H] < -2.5$ exhibit high carbon enhancements $[C/Fe] > +1.0$. It should be kept in mind that these values are not unbiased estimates of the fractions of CEMP stars, rather, they indicate the efficacy of our new approach for the identification of likely carbon-enhanced stars.

We plan to continue our survey for unrecognized CEMP stars, based on this new selection scheme, with the goal of reaching a total sample of ~ 1000 such stars. In the past, CEMP stars were either selected as (1) candidate metal-poor stars from the HK survey or HES based on the apparent weakness of their CaII K lines (and then later found to be CEMP stars based on medium-resolution spectroscopic follow-up), or (2) were selected as carbon-rich stars on the basis of the *sum* of various carbon features in their prism spectra (Christlieb et al. 2001). Both of these techniques have limitations. Technique (1) clearly misses warmer CEMP stars with metallicity $[Fe/H] > -2.5$, and (due to the color range used in the selection) misses CEMP stars with estimated $B-V > 0.9$, as the presence of strong lines of carbon “reddens” the inferred colors outside of the selection window. Technique (2) identifies mostly very cool carbon-rich stars, since it targets a threshold for the total strength of carbon features in a stellar spectrum. Even stars with quite strong CH G-bands often fail to meet the selection threshold, if they are warm enough to not exhibit CN and C₂ bands.

The expanded list of CEMP stars we seek to identify will enable more detailed studies at high spectral resolution, in order to assign them into their proper sub-classes, and to determine the full set of elemental abundances needed in order to explore the astrophysical sites associated with the carbon production.

V.M.P. acknowledges hospitality at the Zentrum für Astronomie der Universität Heidelberg, Landessternwarte, during which the visual inspection of the new CEMP candidates took place. V.M.P. and S.R. ac-

knowledge CNPq, CAPES (PROEX), FAPESP funding (2007/04356-3) and JINA. C.R.K., T.C.B., Y.S.L. and T.S. acknowledge partial support for this work from grants AST 07-07776, PHY 02-15783 and PHY 08-22648;

Physics Frontier Center/Joint Institute for Nuclear Astrophysics (JINA), awarded by the US National Science

REFERENCES

- Allende Prieto, C., et al. 2008, AJ, 136, 2070
 Alvarez, R., & Plez, B. 1998, A&A, 330, 1109
 Aoki, W., Beers, T. C., Christlieb, N., Norris, J. E., Ryan, S. G., & Tsangarides, S. 2007, ApJ, 655, 492
 Barklem, P. S., et al. 2005, A&A, 439, 129
 Beers, T. C., Preston, G. W. & Schectman, S. A. 1985, AJ, 90, 2089
 Beers, T. C., Preston, G. W. & Schectman, S. A. 1992, AJ, 103, 1987
 Beers, T. C., Rossi, S., Norris, J. E., Ryan, S. G., & Sheffler, T. 1999, AJ, 117, 981
 Beers, T. C. & Christlieb, N. 2005, ARA&A, 43, 531
 Campbell, S. W., & Lattanzio, J. C. 2008, A&A, 490, 769
 Cardiel, N., Gorgas, J., Cenarro, J., & Gonzalez, J. J. 1998, A&AS, 127, 597
 Carollo, D., et al. 2007, Nature, 450, 1020
 Castelli, F., & Kurucz, R. L. 2003, Modelling of Stellar Atmospheres, 210, 20P
 Christlieb, N., Green, P. J., Wisotzki, L., & Reimers, D. 2001, A&A, 375, 366
 Christlieb, N., et al. 2002, Nature, 419, 904
 Christlieb, N. 2003, Reviews in Modern Astronomy, 16, 191
 Christlieb, N., et al. 2004, A&A, 428, 1027
 Christlieb, N., Schörck, T., Frebel, A., Beers, T. C., Wisotzki, L., & Reimers, D. 2008, A&A, 484, 721
 Cohen, J. G., et al. 2005, ApJ, 633, L109
 Frebel, A., et al. 2005, Nature, 434, 871
 Frebel, A., et al. 2006, ApJ, 652, 1585
 Goswami, A., Aoki, W., Beers, T. C., Christlieb, N., Norris, J. E., Ryan, S. G., & Tsangarides, S. 2006, MNRAS, 372, 343
 Herwig, F. 2004, ApJS, 155, 651
 Herwig, F. 2005, ARA&A, 43, 435
 Lau, H. H. B., Stancliffe, R. J., & Tout, C. A. 2009, MNRAS, 396, 1046
 Lee, Y. S., et al. 2008, AJ, 136, 205
 Lee, Y. S., et al. 2008, AJ, 136, 2022
 Lucatello, S., Beers, T. C., Christlieb, N., Barklem, P. S., Rossi, S., Marsteller, B., Sivarani, T., & Lee, Y. S. 2006, ApJ, 652, L37
 Marsteller, B. E. 2007, Ph.D. Thesis, Michigan State University
 Masseron, T., et al. 2006, A&A, 455, 1059
 Norris, J. E., Christlieb, N., Korn, A. J., Eriksson, K., Bessell, M. S., Beers, T. C., Wisotzki, L., & Reimers, D. 2007, ApJ, 670, 774
 Reimers, D. 1990 The Messenger, 60, 13
 Reimers, D., & Wisotzki, L. 1997, The Messenger, 88, 14
 Rossi, S., Beers, T. C., Sneden, C., Sevastyanenko, T., Rhee, J., & Marsteller, B. 2005, AJ, 130, 2804
 Schuler, S. C., Margheim, S. J., Sivarani, T., Asplund, M., Smith, V. V., Cunha, K., & Beers, T. C. 2008, AJ, 136, 2244
 Skrutskie, M. F., et al. 2006, AJ, 131, 1163
 Sivarani, T., et al. 2006, A&A, 459, 125
 Stancliffe, R. J., & Glebbeek, E. 2008, MNRAS, 389, 1828
 Tumlinson, J. 2007, ApJ, 664, L63
 York, D. G., et al. 2000, AJ, 120, 1579
 Wisotzki, L., Christlieb, N., Bade, N., Beckmann, V., Köhler, T., Vanelle, C., & Reimers, D. 2000, A&A, 358, 77

TABLE 3
STELLAR DATA FOR THE OBSERVED CANDIDATES

Name	α (J2000)	δ (J2000)	BHES	$(J-K)_0$	GPE (Å)	KPHES (Å)	GPHES (Å)	Tag
HE 0008+0049	00:11:10.5	+01:05:51	14.5	0.58	32.0	7.2	4.7	mpcb
HE 0024-0550	00:26:33.7	-05:33:35	14.7	0.42	30.4	6.0	3.2	mpcc
HE 0034-0011	00:36:51.2	+00:05:29	15.0	0.36	29.7	5.5	5.2	mpcc
HE 0035-5803	00:37:27.3	-57:47:27	15.0	0.36	31.3	7.4	4.1	mpcc
HE 0053-0356	00:56:04.7	-03:40:40	14.7	0.38	36.5	6.1	6.1	mpcb
HE 0058+0141	01:01:16.5	+01:57:46	15.0	0.26	28.6	6.4	2.4	mpcb
HE 0100-4957	01:02:13.8	-49:41:29	15.0	0.58	37.8	7.7	2.8	mpcc
HE 0102-0004	01:05:09.8	+00:11:38	14.3	0.32	29.3	6.1	3.9	mpcb
HE 0118-4834	01:20:18.4	-48:19:12	14.7	0.37	37.4	5.4	5.5	mpcb
HE 0156-5608	01:58:38.8	-55:54:25	14.9	0.49	30.7	6.8	5.0	mpcc
HE 0159-5216	02:01:40.6	-52:02:15	14.7	0.49	32.6	7.5	5.4	mpcc
HE 0214-0818	02:16:44.1	-08:04:31	14.8	0.31	32.9	6.8	4.0	mpcb
HE 0307-5339	03:08:42.2	-53:28:20	14.9	0.44	43.5	7.3	7.6	mpcb
HE 0316-2903	03:18:14.7	-28:52:51	14.7	0.47	37.8	6.7	5.9	mpcc
HE 0320-1242	03:23:07.3	-12:31:27	15.0	0.42	38.1	6.9	3.9	mpcb
HE 0322-3720	03:24:27.8	-37:09:57	14.2	0.62	39.9	7.9	5.5	mpcb
HE 0336-3948	03:38:43.3	-39:38:22	14.9	0.37	30.7	6.0	5.0	mpcc
HE 0340-3933	03:41:56.5	-39:24:06	14.6	0.34	33.0	6.6	4.0	mpcc
HE 0345+0006	03:48:19.4	+00:15:10	15.1	0.53	30.6	6.6	4.0	mpcc
HE 0405-4411	04:07:14.2	-44:03:53	15.1	0.32	31.8	6.9	1.7	unid
HE 0414-4645	04:16:10.2	-46:38:17	15.1	0.34	34.1	5.7	3.4	mpcc
HE 0440-5525	04:42:00.1	-55:19:30	15.0	0.34	32.0	6.4	4.1	mpcb
HE 0444-3536	04:46:39.5	-35:31:07	14.7	0.49	43.2	7.7	6.3	mpcc
HE 0449-1617	04:52:01.4	-16:12:11	15.1	0.42	31.7	6.7	3.8	mpcb
HE 0451-3127	04:53:45.5	-31:22:18	15.1	0.50	30.4	6.6	4.4	mpcc
HE 0500-5603	05:01:41.2	-55:58:46	14.7	0.80	35.6	7.9	5.8	mpcc
HE 0509-1611	05:11:30.0	-16:07:43	15.1	0.52	41.7	7.8	7.1	mpcc
HE 0511-3411	05:13:40.7	-34:08:16	15.0	0.37	33.1	6.4	4.5	mpcc
HE 0514-5449	05:15:11.9	-54:46:21	15.0	0.31	31.0	6.3	3.2	mpcb
HE 0518-3941	05:20:23.1	-39:38:18	14.6	0.18	30.9	6.0	2.5	mpcc
HE 0535-4842	05:36:51.6	-48:40:50	14.7	0.39	30.5	7.8	5.1	unid
HE 0536-5647	05:37:18.1	-56:46:08	14.1	0.49	31.5	7.4	4.1	mpcb
HE 0537-4849	05:38:39.1	-48:47:36	14.9	0.39	30.5	7.8	4.0	mpcb
HE 0901-0003	09:03:53.6	+00:15:48	15.1	0.43	31.1	7.5	4.6	mpcc
HE 0910-0126	09:13:26.1	-01:39:19	14.8	0.26	28.8	4.5	2.9	mpcb
HE 0912+0200	09:15:30.1	+01:47:29	15.1	0.50	45.4	7.6	8.9	mpcc
HE 0918-0156	09:21:06.2	-02:08:58	15.1	0.84	53.2	7.9	7.7	mpcc
HE 0922-0337	09:25:15.3	-03:50:36	14.7	0.61	33.3	8.0	5.1	mpcc
HE 0923-0323	09:26:00.7	-03:36:57	15.1	0.39	30.2	7.8	5.0	mpcc
HE 0928+0003	09:30:33.2	+00:10:08	14.9	0.75	68.0	7.3	8.0	unid
HE 0928+0059	09:31:07.0	+00:46:43	14.8	0.27	30.9	7.5	4.4	mpcb
HE 0933-0733	09:36:09.5	-07:46:57	15.1	0.38	41.5	7.8	6.0	mpcb
HE 0934-1058	09:36:33.7	-11:11:42	14.9	0.67	44.8	7.9	6.1	fhlc
HE 0948+0107	09:51:27.8	+00:53:21	14.9	0.50	31.6	5.8	3.6	mpcb
HE 0948-0234	09:51:09.5	-02:48:21	15.1	0.37	34.0	7.6	4.4	mpcb
HE 0950-0401	09:52:43.7	-04:16:03	14.1	0.34	36.3	6.4	5.7	mpcb
HE 0950-1248	09:53:04.3	-13:03:07	15.0	0.38	33.7	7.0	4.8	mpcc
HE 0951+0114	09:53:55.5	+01:00:29	14.9	0.63	59.9	7.8	5.5	mpcb
HE 1001-1621	10:03:54.8	-16:35:45	15.0	0.40	34.4	6.2	4.5	mpcc
HE 1002-1405	10:04:35.4	-14:19:54	14.1	0.36	38.8	7.5	4.9	mpcc
HE 1007-1524	10:09:38.2	-15:39:20	15.0	0.36	32.3	6.9	4.6	mpcc
HE 1009-1342	10:12:10.0	-13:57:17	15.0	0.85	62.7	8.0	5.5	unid
HE 1009-1613	10:11:26.5	-16:28:40	14.4	0.40	39.6	7.0	6.9	mpcc
HE 1009-1646	10:12:11.5	-17:01:17	15.1	0.40	39.2	6.6	7.5	mpcc
HE 1010-1445	10:13:03.8	-15:00:51	15.0	0.56	30.6	6.9	5.8	mpcc
HE 1022-0730	10:24:39.3	-07:45:59	14.9	0.37	30.2	7.7	5.3	mpcb
HE 1027-1217	10:29:29.9	-12:32:31	15.1	0.43	35.2	5.4	3.1	mpcb
HE 1028-1505	10:31:23.4	-15:20:46	15.0	0.62	33.5	7.8	4.4	mpcc
HE 1039-1019	10:42:25.4	-10:34:51	14.9	0.40	36.2	7.8	4.8	mpcb
HE 1045+0226	10:48:03.4	+02:10:47	15.0	0.57	53.6	7.4	8.9	mpcb
HE 1046-1644	10:49:13.4	-17:00:19	14.7	0.55	30.2	7.0	4.4	mpcb
HE 1049-0922	10:52:26.2	-09:38:33	14.7	0.58	48.4	8.0	5.5	unid
HE 1049-1025	10:51:44.2	-10:41:05	14.1	0.45	54.7	7.4	9.6	mpcb
HE 1104-0238	11:07:00.4	-02:54:17	15.0	0.90	33.8	7.9	5.5	unid
HE 1110-1625	11:13:05.4	-16:41:29	15.0	0.38	33.4	6.9	5.4	mpcc
HE 1112-0203	11:14:48.6	-02:19:26	14.2	0.83	45.3	7.9	5.9	unid
HE 1125-1343	11:28:26.1	-13:59:58	15.0	0.66	36.1	7.1	5.4	mpcc
HE 1129-1405	11:32:19.2	-14:21:44	15.1	0.48	33.0	6.5	4.9	mpcc
HE 1132-0915	11:35:24.9	-09:32:33	14.7	0.39	31.8	4.8	3.4	mpcc
HE 1133-0802	11:35:59.0	-08:18:43	14.9	0.49	40.4	8.0	7.1	mpcc
HE 1135-0800	11:38:23.9	-08:16:57	15.1	0.54	32.7	6.0	4.9	mpcb
HE 1137-1259	11:39:37.2	-13:15:52	15.0	0.58	35.0	7.3	5.3	mpcb
HE 1142-0637	11:45:00.8	-06:54:18	14.9	0.57	34.3	7.4	3.8	mpcc
HE 1146-1040	11:49:24.5	-10:56:41	15.0	0.50	40.9	7.6	5.4	mpcc
HE 1146-1126	11:49:09.5	-11:43:02	14.9	0.58	34.9	6.5	5.3	mpcc

TABLE 3 — *Continued*

Name	α (J2000)	δ (J2000)	BHES	$(J-K)_0$	GPE (\AA)	KPHES (\AA)	GPHES (\AA)	Tag
HE 1147–1057	11:49:33.0	–11:14:26	15.1	0.38	33.2	5.7	4.4	mpcb
HE 1148–1020	11:51:11.4	–10:37:32	15.0	0.41	36.2	7.7	3.6	mpcb
HE 1148–1025	11:50:49.8	–10:41:42	14.8	0.42	38.5	6.9	6.1	mpcb
HE 1212–1123	12:14:36.7	–11:39:48	15.1	0.29	31.5	6.2	3.9	mpcb
HE 1217–1054	12:19:56.9	–11:11:27	14.9	0.55	38.3	7.6	6.0	mpcc
HE 1217–1633	12:20:30.2	–16:49:44	14.8	0.52	56.5	7.7	9.7	fhlc
HE 1222–1631	12:24:59.5	–16:48:15	14.8	0.57	34.1	7.7	5.7	mpcc
HE 1223–0930	12:26:01.9	–09:47:35	14.5	0.50	45.8	7.4	8.2	fhlc
HE 1224–0723	12:27:15.1	–07:40:21	14.9	0.41	38.9	6.7	5.1	mpcc
HE 1224–1043	12:26:51.5	–11:00:35	14.8	0.36	33.5	4.8	2.5	mpcc
HE 1228–0750	12:31:30.3	–08:06:38	15.0	0.30	30.3	4.8	1.9	mpcb
HE 1228–1438	12:30:44.6	–14:55:05	14.5	0.89	42.6	8.0	7.9	mpcb
HE 1231–3136	12:34:31.2	–31:52:39	15.1	0.33	30.3	5.6	2.2	mpcb
HE 1255–2734	12:58:18.4	–27:50:23	14.3	0.43	36.8	5.6	5.9	mpcc
HE 1301+0014	13:03:45.8	+00:01:28	15.1	0.46	32.6	5.2	3.3	mpcc
HE 1301–1405	13:04:03.6	–14:21:30	15.1	0.48	34.3	6.7	4.8	mpcc
HE 1302–0954	13:04:58.2	–10:10:11	14.5	0.49	32.8	7.4	5.1	mpcb
HE 1311–3002	13:13:59.7	–30:18:21	14.3	0.58	34.8	8.0	7.2	fhlc
HE 1320–1130	13:23:37.0	–11:46:03	15.1	0.34	34.4	7.0	4.7	mpcb
HE 1320–1641	13:23:11.9	–16:56:38	15.0	0.87	43.5	7.9	6.9	mpcc
HE 1321–1652	13:24:27.3	–17:07:48	15.0	0.35	43.3	5.8	7.1	mpcc
HE 1343+0137	13:46:17.3	+01:22:29	15.1	0.41	28.3	5.5	2.5	mpcc
HE 1408–0444	14:10:50.4	–04:58:51	14.7	0.22	31.2	2.2	2.8	mpcb
HE 1409–1134	14:11:43.4	–11:49:02	15.0	0.36	36.4	7.9	4.3	mpcb
HE 1410–0549	14:13:21.7	–06:03:33	14.9	0.25	31.0	6.1	1.4	mpcb
HE 1414–1644	14:17:03.4	–16:58:23	14.6	0.47	32.8	6.0	4.7	mpcc
HE 1418–1634	14:20:51.0	–16:47:46	15.1	0.54	30.5	7.0	6.1	mpcc
HE 1428–0851	14:30:40.6	–09:05:09	14.9	0.53	30.5	6.2	2.4	mpcc
HE 1430–1518	14:32:56.4	–15:31:35	14.9	0.79	45.9	7.6	10.1	unid
HE 1447–1533	14:49:54.5	–15:46:22	14.3	0.83	34.5	7.9	6.9	mpcc
HE 1448–1406	14:50:53.1	–14:19:14	14.9	0.37	30.4	5.8	2.7	mpcb
HE 1451–0659	14:54:03.0	–07:11:40	14.5	0.63	37.0	7.9	5.6	mpcb
HE 1458–0923	15:00:45.4	–09:35:49	14.4	0.41	47.9	6.6	6.9	mpcb
HE 1458–1022	15:01:35.7	–10:33:54	14.7	0.54	30.2	7.0	5.3	mpcc
HE 1458–1226	15:01:32.8	–12:37:57	15.1	0.47	43.5	7.4	6.9	mpcc
HE 1504–1534	15:07:46.2	–15:45:31	14.8	0.85	38.9	8.0	7.3	mpcc
HE 1505–0826	15:08:04.7	–08:38:22	14.9	0.25	32.2	7.5	3.6	mpcb
HE 1507–1055	15:10:09.9	–11:07:19	14.9	0.80	39.3	7.8	8.8	mpcc
HE 1507–1104	15:09:45.4	–11:16:09	15.1	0.90	46.3	7.3	8.3	mpcb
HE 1512+0149	15:15:08.3	+01:38:05	15.0	0.67	54.6	7.1	8.7	mpcc
HE 1516–0107	15:18:54.0	–01:18:50	15.0	0.43	35.1	5.0	4.5	mpcb
HE 1518–0541	15:21:20.6	–05:52:08	14.1	0.54	32.4	6.8	3.5	mpcb
HE 1527–0740	15:30:18.5	–07:50:50	15.1	0.44	37.8	6.2	1.7	mpcb
HE 1529–0838	15:31:54.8	–08:48:39	15.1	0.38	36.4	7.9	4.9	mpcb
HE 2025–5221	20:29:38.6	–52:11:22	14.8	0.39	39.1	4.7	6.1	mpcc
HE 2052–5610	20:56:34.9	–55:59:17	15.0	0.27	39.9	6.0	7.0	mpcc
HE 2112–5236	21:16:09.2	–52:23:30	14.8	0.52	43.5	7.1	7.0	mpcc
HE 2117–6018	21:21:26.2	–60:05:33	15.0	0.59	31.7	6.6	4.9	mpcc
HE 2140–4746	21:44:06.1	–47:32:59	14.7	0.36	30.6	5.8	3.1	mpcc
HE 2151–0332	21:53:58.6	–03:18:09	15.0	0.47	40.0	5.7	5.1	mpcb
HE 2201–1108	22:04:08.4	–10:53:33	15.0	0.29	39.3	6.0	4.2	mpcb
HE 2207–0912	22:10:13.4	–08:57:29	15.0	0.41	36.8	4.3	1.5	mpcc
HE 2209–1212	22:11:44.1	–11:57:37	14.6	0.30	39.8	5.1	4.3	mpcb
HE 2219–1357	22:22:28.2	–13:42:06	14.9	0.20	30.3	4.4	2.3	mpcb
HE 2231–0710	22:33:56.1	–06:54:35	14.6	0.43	57.4	1.2	7.7	mpcb
HE 2257–5710	23:00:40.4	–56:54:15	14.7	0.51	31.6	6.6	5.3	mpcc
HE 2353–5329	23:55:49.3	–53:12:39	13.9	0.29	33.0	4.6	4.1	mpcc

TABLE 4
ATMOSPHERIC PARAMETERS AND CARBON ABUNDANCE ESTIMATES FOR THE
OBSERVED CANDIDATES.

Name	V (km/s)	σ_V (km/s)	T_{eff} (K)	$\log g$ (cgs)	[Fe/H]	[C/Fe] ^a	$\sigma_{[\text{C}/\text{Fe}]}$
HE 0008+0049	-27.6	13.3	5054	4.27	-1.73	0.26	0.13
HE 0024-0550	80.6	7.2	5761	4.39	-1.94	0.44	0.06
HE 0034-0011	-173.0	18.3	6111	4.39	-2.16	1.73	0.13
HE 0035-5803	78.7	25.7	6083	4.57	-0.65	1.00	0.05
HE 0053-0356	-5.8	13.6	6004	4.39	-1.98	1.73	0.13
HE 0058+0141	17.1	10.5	6670	4.57	-0.46	0.77	0.07
HE 0100-4957	184.2	17.2	5050	2.61	-2.32	-0.11	0.20
HE 0102-0004	-106.2	13.2	6314	3.93	-2.20	1.19	0.19
HE 0118-4834	-86.0	28.0	6015	4.50	-2.34	2.09	0.25
HE 0156-5608	279.0	8.1	5431	4.32	-2.02	0.77	0.06
HE 0159-5216	42.3	8.0	5413	3.80	-1.90	0.77	0.09
HE 0214-0818	46.6	4.7	6379	4.34	-1.12	1.25	0.09
HE 0307-5339	207.5	37.1	5689	4.32	-1.96	1.06	0.25
HE 0316-2903	269.3	21.4	5528	4.43	-2.29	1.04	0.13
HE 0320-1242	123.8	14.3	5745	4.39	-0.88	0.17	0.20
HE 0322-3720	-3.5	21.3	4901	4.71	-0.96	0.10	0.20
HE 0336-3948	165.3	2.7	6066	4.52	-0.64	0.44	0.07
HE 0340-3933	-1.1	6.2	6226	4.57	-0.28	0.06	0.20
HE 0345+0006	17.2	13.2	5262	3.32	-2.50	0.18	0.06
HE 0405-4411	126.1	11.3	6337	4.05	-1.14	0.89	0.13
HE 0414-4645	92.0	24.8	6197	4.59	-1.02	0.77	0.06
HE 0440-5525	87.3	25.2	6186	4.25	-1.18	0.52	0.19
HE 0444-3536	181.6	16.4	5417	3.96	-1.57	1.16	0.13
HE 0449-1617	116.7	15.0	5756	4.50	-1.07	0.06	0.20
HE 0451-3127	342.4	26.2	5373	3.59	-2.97	1.13	0.13
HE 0500-5603	156.0	23.6	4273	1.64	-1.61	-0.50	0.20
HE 0509-1611	114.7	22.3	5279	3.80	-1.03	0.36	0.13
HE 0511-3411	98.9	34.3	6055	4.57	-0.44	0.38	0.05
HE 0514-5449	182.7	8.4	6414	4.16	-0.86	0.32	0.20
HE 0518-3941	58.7	36.4	7153	3.34	-0.49	1.00	0.20
HE 0535-4842	78.3	21.0	5910	4.43	-0.99	0.48	0.13
HE 0536-5647	180.3	22.5	5417	4.02	-1.39	-0.12	0.20
HE 0537-4849	92.9	23.3	5938	4.71	-0.30	0.10	0.20
HE 0901-0003	30.4	20.0	5720	4.64	-0.69	0.88	0.13
HE 0910-0126	197.4	16.9	6694	3.89	-1.92	1.03	...
HE 0912+0200	83.5	15.2	5395	4.48	-0.75	-0.09	0.20
HE 0918-0156	99.6	16.8	4237	1.61	-1.12	0.18	0.20
HE 0922-0337	78.3	62.2	4943	4.14	-1.38	-0.14	0.20
HE 0923-0323	127.9	17.7	5905	4.27	-0.48	0.46	0.27
HE 0928+0003	-133.9	70.5	4402	4.09	-1.14	-0.11	0.20
HE 0928+0059	13.6	7.8	6598	4.39	-0.83	0.59	0.09
HE 0933-0733	61.7	16.7	5982	4.39	-1.03	0.77	0.14
HE 0934-1058	-406.9	37.1	4702	3.14	-1.77	-0.50	0.25
HE 0948+0107	514.9	5.2	5382	4.46	-2.14	0.20	0.06
HE 0948-0234	147.3	54.4	6021	4.55	-0.44	0.38	0.19
HE 0950-0401	144.0	14.4	6197	4.46	-1.62	2.01	0.13
HE 0950-1248	87.6	18.3	5982	4.41	-0.30	0.10	0.20
HE 0951+0114	-255.2	32.9	4882	4.61	-1.32	-0.50	0.20
HE 1001-1621	-10.4	26.2	5888	4.30	-0.92	0.17	0.20
HE 1002-1405	99.2	9.5	6077	4.50	-0.44	0.38	0.05
HE 1007-1524	96.5	18.3	6077	4.43	-0.64	0.46	0.19
HE 1009-1342	-154.3	17.3	4242	4.30	-1.72	0.02	0.20
HE 1009-1613	91.0	11.8	5883	4.34	-0.67	0.84	0.15
HE 1009-1646	21.3	39.6	5883	4.46	-0.70	0.41	0.13
HE 1010-1445	202.0	14.0	5117	3.43	-0.89	-0.03	0.20
HE 1022-0730	110.3	11.4	6060	4.41	-1.58	0.99	0.13
HE 1027-1217	146.6	27.5	5720	2.00	-1.49
HE 1028-1505	65.4	33.9	4886	3.84	-0.57	0.04	0.20
HE 1039-1019	117.1	12.4	5878	4.55	-0.67	0.92	0.08
HE 1045+0226	214.2	21.5	5109	1.90	-3.05	2.30	0.25
HE 1046-1644	-39.5	25.6	5168	3.02	-0.60	0.19	0.20
HE 1049-0922	-34.7	30.3	5074	4.71	-0.63	0.33	0.20
HE 1049-1025	-175.7	43.4	5634	4.50	-0.78	-0.50	0.20
HE 1104-0238	166.8	24.0	4450	1.77	-0.94	-0.5	0.05
HE 1110-1625	123.5	17.7	5998	4.46	-0.30	0.11	0.20
HE 1112-0203	8.8	41.0	4235	4.23	-0.91	-0.50	0.20
HE 1125-1343	-169.4	33.2	4752	4.48	-1.02	-0.03	0.20
HE 1129-1405	189.3	41.7	5476	3.34	-2.02	0.60	0.09
HE 1132-0915	51.5	41.7	5905	2.00	-1.56
HE 1133-0802	27.5	13.9	5431	4.07	-1.40	0.57	0.06
HE 1135-0800	221.3	7.8	5225	3.05	-2.28	0.08	0.03
HE 1137-1259	138.1	23.5	5050	4.64	-1.05	0.16	0.20
HE 1142-0637	118.4	24.3	5089	4.14	-1.58	-0.04	0.20
HE 1146-1040	-15.0	27.2	5382	4.57	-1.18	0.37	0.05
HE 1146-1126	332.1	14.1	5062	2.84	-2.26	0.00	0.20

TABLE 4 — *Continued*

Name	V (km/s)	σ_V (km/s)	T_{eff} (K)	$\log g$ (cgs)	[Fe/H]	[C/Fe] ^a	$\sigma_{[\text{C}/\text{Fe}]}$
HE 1147–1057	113.9	10.6	5971	4.52	−0.89	0.42	0.06
HE 1148–1020	238.6	19.3	5835	4.39	−1.34	0.15	0.20
HE 1148–1025	194.6	28.6	5792	4.52	−0.83	0.03	0.20
HE 1212–1123	111.6	21.8	6503	4.07	−1.35	0.93	0.06
HE 1217–1054	60.2	34.9	5156	4.57	−0.96	−0.02	0.20
HE 1217–1633	155.6	24.6	5300	3.27	−1.90	1.03	0.38
HE 1222–1631	104.6	13.7	5101	3.05	−2.07	0.18	0.06
HE 1223–0930	187.0	14.0	5377	3.43	−2.19	1.76	0.19
HE 1224–0723	64.9	24.7	5803	4.57	−0.67	0.84	0.15
HE 1224–1043	303.0	21.9	6094	3.32	−1.67	−0.08	0.20
HE 1228–0750	353.6	14.1	6444	3.68	−1.60	0.40	0.20
HE 1228–1438	176.1	19.5	4434	2.27	−0.92	−0.50	0.05
HE 1231–3136	81.9	49.2	6279	3.59	−1.51	0.99	0.06
HE 1255–2734	−21.2	34.6	5730	4.43	−2.14	1.30	0.13
HE 1301+0014	72.0	19.5	5571	3.61	−2.37	0.44	0.06
HE 1301–1405	43.0	7.9	5467	3.41	−1.29	−0.11	0.20
HE 1302–0954	145.7	22.9	5417	4.00	−2.30	0.77	0.13
HE 1311–3002	213.6	27.8	5043	2.86	−2.39	0.64	0.09
HE 1320–1130	220.8	41.9	6238	4.39	−1.62	1.37	0.08
HE 1320–1641	84.1	14.5	4295	1.73	−1.03	−0.28	0.20
HE 1321–1652	91.1	41.0	6169	4.61	−1.72	2.13	0.25
HE 1343+0137	130.6	19.5	5808	3.23	−1.73	−0.02	0.20
HE 1408–0444	142.5	27.9	6912	3.09	−2.38	1.79	...
HE 1409–1134	92.2	12.9	6117	4.43	−0.37	0.23	0.20
HE 1410–0549	103.8	25.9	6742	2.21	−1.70
HE 1414–1644	91.8	11.8	5514	4.23	−2.46	0.70	0.04
HE 1418–1634	144.3	39.1	5196	2.91	−2.28	0.12	0.06
HE 1428–0851	91.3	22.4	5241	1.68	−2.52	−0.48	...
HE 1430–1518	383.0	26.2	4289	1.93	−1.16	0.41	0.08
HE 1447–1533	57.1	24.3	4234	2.07	−1.05	0.13	0.20
HE 1448–1406	−173.8	22.7	6060	2.36	−1.67	0.10	0.20
HE 1451–0659	−22.9	57.5	4882	4.64	−1.47	−0.11	0.20
HE 1458–0923	−343.0	27.3	5829	4.39	−2.27	1.89	0.13
HE 1458–1022	−61.3	18.2	5200	3.09	−2.22	0.47	0.06
HE 1458–1226	−10.1	30.5	5504	4.68	−1.05	0.39	0.13
HE 1504–1534	60.3	6.9	4246	1.41	−0.73	0.32	0.06
HE 1505–0826	69.2	18.4	6730	4.39	−0.49	0.48	0.20
HE 1507–1055	174.0	16.0	4267	1.66	−1.14	0.18	0.20
HE 1507–1104	124.1	12.0	4492	2.91	−0.98	−0.01	0.20
HE 1512+0149	−65.3	41.2	4706	4.57	−0.94	−0.50	0.20
HE 1516–0107	16.9	28.5	5720	3.77	−2.01	0.65	0.03
HE 1518–0541	32.1	30.1	5217	4.68	−1.03	0.13	0.20
HE 1527–0740	27.4	28.4	5679	2.00	−1.86	0.26	...
HE 1529–0838	38.7	24.6	5960	4.52	−0.69	0.57	0.19
HE 2025–5221	237.5	19.7	5932	4.57	−2.25	2.00	0.25
HE 2052–5610	281.7	35.8	6628	4.59	−1.76	2.69	0.05
HE 2112–5236	254.5	15.0	5304	3.93	−1.79	0.76	0.19
HE 2117–6018	−205.1	30.6	5023	4.11	−1.93	−0.17	0.20
HE 2140–4746	70.8	14.7	6111	4.36	−1.36	0.49	0.06
HE 2151–0332	−99.6	21.0	5514	4.30	−2.75	1.45	0.19
HE 2201–1108	−115.3	19.0	6533	4.07	−0.95	0.79	0.19
HE 2207–0912	−67.2	13.7	5824	4.30	−2.40	0.81	0.13
HE 2209–1212	107.8	30.7	6432	4.43	−0.38	0.26	0.20
HE 2219–1357	133.0	14.4	7082	4.25	−0.64	0.72	0.20
HE 2231–0710	63.1	34.4	5704	2.86	−0.61	0.72	0.29
HE 2257–5710	41.6	17.2	5343	3.89	−2.97	1.22	0.06
HE 2353–5329	105.3	12.6	6509	4.57	−1.75	2.35	0.13

^a The [C/Fe] values with no errors associated are upper limits.